OPTICA

Global phase diagram of bound states in the continuum

PENG HU,[1,†] JIAJUN WANG,[2,†] QIAO JIANG,[1,3] ● JUN WANG,[1] LEI SHI,[2,5] ● DEZHUAN HAN,[1,*] ●
Z. Q. ZHANG,[4] C. T. CHAN,[4] AND JIAN ZI[2,6]

[1]*College of Physics, Chongqing University, Chongqing 401331, China*
[2]*State Key Laboratory of Surface Physics, Key Laboratory of Micro- and Nano-Photonic Structures (Ministry of Education) and Department of Physics, Fudan University, Shanghai 200433, China*
[3]*Chongqing Key Laboratory for Strongly Coupled Physics, Chongqing University, Chongqing 401331, China*
[4]*Department of Physics, Hong Kong University of Science and Technology, Clear Water Bay, Hong Kong, China*
[5]*e-mail: lshi@fudan.edu.cn*
[6]*e-mail: jzi@fudan.edu.cn*
*Corresponding author: dzhan@cqu.edu.cn

Bound states in the continuum (BICs) in photonic-crystal slabs have been conventionally classified into three types: single-resonance parametric, symmetry-protected, and Friedrich–Wintgen BICs. Here, we show that the single-resonance parametric BICs come from the coupling between the guided resonance (GR) and Fabry–Perot (FP) modes, and the symmetry-protected BICs from the coupling between degenerate GR modes. Hence, the three types of BICs in photonic-crystal slabs can be classified by the three different Friedrich–Wintgen origins. Based on this universal classification, a global phase diagram of BICs can be obtained with each phase identified by the indices of the three different Friedrich–Wintgen-type BICs. When BICs are created or annihilated, a phase transition occurs and is experimentally observed, in which the FP modes play a significant role. Our work shows a clear physical picture on whether BICs exist and how sensitive they are to changes in the parameter space, and enables improvements in experiment design and applications. © 2022 Optica Publishing Group under the terms of the Optica Open Access Publishing Agreement

1. INTRODUCTION

Bound states in the continuum (BICs) are a special type of resonance state with an infinite lifetime [1–3]. They coexist with extended states in free space. Both of them have the same momentum and energy, but are not coupled to each other. In 1929, von Neuman and Wigner established the concept of BIC by constructing a quantum-mechanical example of a potential that is oscillatory and decays slowly to zero at infinity [4]. Yet later, BICs were found to be a wave phenomenon widely existing in quantum [5], photonic [6–28], acoustic [29], and plasmonic systems [30]. According to the formation mechanism, all of the BICs discovered up to now are divided into four types [1,3]. The first type is the single-resonance parametric BIC evolving from a single-resonance mode when the radiation of its constituent components is destructively interfered [6–18]. The second type is the symmetry-protected BIC, which is caused by the symmetry mismatch between it and the extended states in the environment [19–22]. The third type is the Friedrich–Wintgen BIC [5,23–25,29,30], which is the result of complete destructive interference of two resonance modes. The fourth type is called the Fabry–Perot (FP) BIC, which is constructed by two separate resonators that form a FP cavity without leakage [26–28]. In this work, we study the evolution of BICs in a single photonic-crystal

(PhC) slab under parameter variations. Since the fourth type BIC is observed in two parallel PhC slabs [27], it is not associated with the BICs in a single slab we study here.

The aim of this work is to establish a framework based on which the creation and annihilation of the BICs as well as their interconversions can all be studied simultaneously. It is well known that all BICs correspond to vortex centers of far-field polarization so that topological charges can be assigned, and also the conservation of total topological charge holds during the evolution of BICs [7–9]. The interconversions of different types of BICs can also be investigated from this topological viewpoint [21–23]. However, the dominant role in the interconversions of different types of BICs and the resultant global phase diagram under parameter variations are yet to be revealed.

In order to establish such a framework, based on the idea of Friedrich–Wintgen BICs [5], we propose a universal classification of BICs in the PhC slab. We show that the three aforementioned types of BICs can be obtained from the interaction of two resonance modes of the slab. There are basically two types of slab modes existing above the light line, which are guided resonance (GR) modes and FP modes [31]. The FP modes were previously considered only as background of the spectrum because of their low Q factors [15,32,33]. Here, we demonstrate that the single-resonance

parametric BIC (the first type) is in fact not a single-resonance mode, but the result of the coupling of a GR mode and a FP mode. This type of BIC is typical in the PhC slab and is also referred to as the accidental BIC [6–9,12–16]. The symmetry-protected BIC (the second type) can be viewed as the result of the coupling of degenerate GR modes at high symmetry points in momentum space. The third type, i.e., the original Friedrich–Wintgen BIC, can be obtained from the coupling of two different GR modes. Thus, all the three types of BICs in PhC slabs can be regarded as Friedrich–Wintgen-type BICs, and can be classified by the above three different origins.

Based on the above universal classification, we further propose a global phase diagram for the BICs in PhC slabs. Each phase is identified by three indices (n_1, n_2, n_3), where $n_i (i = 1, 2, 3)$ denotes the number of BICs with the ith type of Friedrich–Wintgen origin in this phase. When a phase transition takes place, BICs can merge, emerge, or disappear in momentum space. Thus, the existence of the different types of BICs and how sensitive they are to the changes in system parameter can be clearly seen in the phase diagram. It should be emphasized that the FP modes in a single slab play a significant role in the evolution of BICs and phase transitions. We have also carried out experiments to observe the critical points of the phase transitions, including the merging process of BICs at the off $- \Gamma$ point. The classification of BICs according to Friedrich–Wintgen origins and the corresponding global phase diagrams not only deepen our understanding of BICs, but also pave the way to their applications.

2. THEORY AND RESULTS

A. Friedrich–Wintgen Origin

Friedrich and Wintgen demonstrated that BICs can occur due to the interference of different resonances [5]. If two resonances have a degeneracy point when we tune some continuous parameter, the interference can cause an avoided level crossing of the frequencies, and a BIC with vanishing resonance width may be formed at some specific value of the continuous parameter. The effective Hamiltonian for an open photonic system has been studied previously [33,34], which is non-Hermitian and can be written as follows:

$$H = H_{\mathrm{B}} - i\Gamma, \tag{1a}$$

$$\Gamma = D^{\dagger} D / 2, \tag{1b}$$

where H_B is a Hermitian operator giving rise to discrete and real eigenvalues for the bound states. When these eigenstates couple to some open channels characterized by the coupling matrix D, the energy will leak out and the eigenvalues of energy are no longer purely real. Γ is the operator that governs the imaginary part of eigenenergy. If the coupling matrix D has a zero eigenvalue; namely there exists a null vector $|\psi_0\rangle$ satisfying

$$D |\psi_0\rangle = 0, \tag{2}$$

and if $|\psi_0\rangle$ is also an eigenvector of H_B, i.e.,

$$H_{\mathrm{B}} |\psi_0\rangle = \omega_0 |\psi_0\rangle, \tag{3}$$

state $|\psi_0\rangle$ is a BIC having a purely real eigenenergy and satisfying $H|\psi_0\rangle = \omega_0|\psi_0\rangle$. Here we adopt natural unit with $\hbar = 1$ so that the energy and frequency have the same natural unit.

For a two-level system, both H_B and Γ become 2×2 matrices. For the case of a PhC slab, optical waves can radiate into both the upper and lower space with two orthogonal polarizations. There exist four open channels in total, and thus D is a 4×2 matrix. An interesting case is that on the high symmetry lines in the Brillouin zone, two polarization degrees of freedom can be considered separately due to the symmetry [35]. Furthermore, if the system has up–down mirror (σ_z) symmetry, the radiation into the upper and lower space is either symmetric or antisymmetric. Therefore the total number of independent open channels can be further reduced to 1. The coupling matrix D becomes a 1×2 matrix, and Eq. (1.2) turns into $\Gamma = D^{\dagger} D$. A null vector satisfying Eq. (2) should exist since the rank of D is less than the number of columns. To be specific, one can set

$$D = \left(e^{i\theta_1} \sqrt{\gamma_1}, \, e^{i\theta_2} \sqrt{\gamma_2} \right), \tag{4}$$

where γ_i and θ_i are the decay rates and the phase angle of radiation of the ith level, respectively. The relative phase angle $\theta_1 - \theta_2$ can be 0 or π [33]. The Hamiltonian in Eq. (1) thus becomes

$$H = \begin{pmatrix} \omega_1 & \kappa \\ \kappa & \omega_2 \end{pmatrix} - i \begin{pmatrix} \gamma_1 & \pm\sqrt{\gamma_1\gamma_2} \\ \pm\sqrt{\gamma_1\gamma_2} & \gamma_2 \end{pmatrix}, \tag{5}$$

where ω_1 and ω_2 are the resonant frequencies, and κ and $\pm\sqrt{\gamma_1\gamma_2}$ are the near-field and the far-field coupling coefficients, respectively. The signs $\pm$ correspond to, respectively, the even and odd symmetries of the two resonance modes. The null vector of Eq. (4) can be easily found:

$$|\psi_0\rangle = \left(\sqrt{\gamma_2}, \mp\sqrt{\gamma_1} \right) / \sqrt{\gamma_1 + \gamma_2}. \tag{6}$$

The condition of BIC requires that this null vector $|\psi_0\rangle$ is also an eigenvector of H_B. According to Eqs. (3) and (5), we obtain

$$\kappa(\gamma_1 - \gamma_2) = \pm\sqrt{\gamma_1\gamma_2}(\omega_1 - \omega_2). \tag{7}$$

Our aim is to demonstrate that the BICs in the PhC slab can be described by a Friedrich–Wintgen-type Hamiltonian in Eq. (1a), or more specifically, Eq. (5). The key point is to determine the energy levels involved in this Hamiltonian. It is commonly believed that the BIC appearing in momentum space with an accidental wave vector k is a single-resonance mode lying on a GR band, which can be interpreted by the destructive interference of the radiation from its constituent waves and achieved by fine-tuning system parameters [1,12–14]. In the following, we first prove that it is the interaction between a FP mode and a GR mode that generates an accidental BIC.

We take a system of one-dimensional PhC slab as an example. Figure 1(a) shows the one-dimensional PhC slab under study with a period of a in the x direction, uniformity in the y direction, and a thickness of h in the z direction. The alternating dielectric layers in the PhC have relative permittivities ε_1 and ε_2, and thicknesses d and $a-d$, respectively. The background medium is air. The basic properties of FP and GR modes such as their dispersions can be investigated from the viewpoint of effective medium theory (EMT) [36] in which the PhC slab is treated as a homogeneous slab with the same thickness and an effective relative permittivity $\varepsilon_{\mathrm{eff}}$. Using the method of the transfer matrix, we can calculate all the photonic modes of this effective medium slab, as shown in Fig. 1(b). There exist two types of modes in fact: guided modes below the light line (solid lines labeled by GM) and FP modes above the light line (dashed lines). It is noted that a small portion
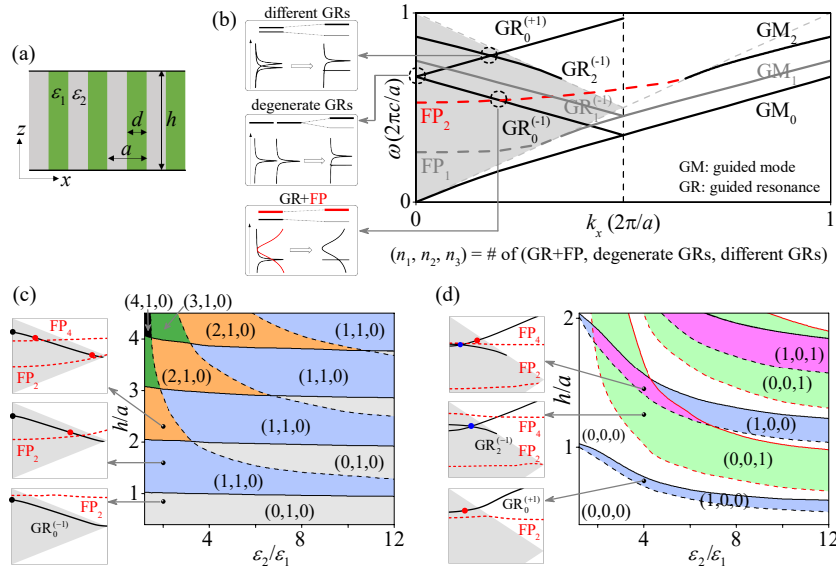
Fig. 1. Global phase diagrams of BICs in the PhC slab. (a) Schematic diagram of the PhC slab. (b) Band diagrams of the effective homogeneous slab of a PhC slab, including guided modes (labeled by GM_n) and FP modes. When a periodic modulation of the dielectric constant is introduced, the GM_n band is folded into the first Brillouin zone and forms a guided resonance band (labeled by $GR_n^{(m)}$). The gray shaded region indicates the region with only one radiation channel. The three insets show the diagrams of Friedrich–Wintgen BICs from three different origins: GR+FP modes, degenerate GR modes, and two different GR modes, including the energy levels before and after coupling of the two modes and the corresponding reflection spectra. (c),(d) Phase diagrams of BICs on $GR_0^{(-1)}$ and $GR_0^{(+1)}$ bands in the first Brillouin zone for TE polarization, respectively. Only the positive k_x axis is considered due to the inversion symmetry. Each phase is indicated by (n_1, n_2, n_3), indices of the three types of Friedrich–Wintgen BICs shown in (b). Solid (dashed) line shows that the BIC emerges or disappears at the Γ point (from the light line or folded light line). Black and red lines represent the critical lines for the BICs resulting from the coupling of the GR and FP modes and BICs resulting from two different GR modes, respectively. Several examples of simulated band diagrams are displayed in the insets to show different BIC phases, where the red, black, and blue dots represent the BICs from GR+FP modes, degenerate GR modes, and two different GR modes, respectively. Here, the other system parameters are chosen as $\varepsilon_1 = 1$ and $d = 0.5a$.

of the FP bands can lie below the light line [37]. If we divide the effective medium slab into unit cells with period a, the dispersion curve of the guided modes will be folded into the first Brillouin zone. Once a finite periodic modulation of dielectric constant is considered, the folded GM mode will transform into a GR mode with a finite decay rate as it couples to the radiation modes. When the periodic modulation is small, the dispersion of a GR mode can be well approximated by that of the corresponding folded GM mode, but its decay rate cannot be given by the EMT. Here, the GR bands are labeled by $GR_n^{(m)}$ (either for TE or TM polarization), which represents the nth-order GR mode with m being the index of band folding in the reduced-zone scheme. In this study, the region with only one radiation channel is considered, as indicated by the gray shaded region in Fig. 1(b).

If we track the accidental BICs in the parameter space, it is found that they are close to the intersection points of the corresponding folded GM and FP bands in the effective medium slab (see Figs. S2 and S3 in Supplement 1 for examples). Here, the folded GM and FP modes should have the same σ_z symmetry. Since the dispersion of the GR mode can be approximated by the corresponding folded GM bands within the framework of EMT, these intersection points can be treated as nearly the avoided crossing points [24,25]. Hence, it can be inferred that the accidental BICs, appearing near the avoided crossing points, are also a type of Friedrich–Wintgen BIC. The non-interacting GR and FP modes serve as the basis vectors of the Hamiltonian in Eq. (5). The interaction between these GR and FP modes modifies not only the eigenenergies but also the eigenstates. In particular, it will give rise to an accidental BIC with no radiation

loss when the condition Eq. (7) is satisfied. Let us use the subscript 1 (2) to denote the GR (FP) mode. Since the FP modes are much more leaky than the GR modes, i.e., $\gamma_1 \ll \gamma_2$, we have that $|\Delta\omega_{1,2}| \triangleq |\omega_1 - \omega_2| \approx |\kappa\sqrt{\gamma_2/\gamma_1}| \gg |\kappa|$ from Eq. (7). This manifests a significant feature of accidental BICs that their deviation from the corresponding avoided crossing points is much larger than the coupling strength of the GR and FP bands. The sign of κ in Eq. (5) determines on which side of the intersection point the BIC will occur.

In order to obtain the effective Hamiltonian in Eq. (5), in what follows a general procedure is employed. The eigenfrequencies of the GR and FP modes in the PhC slab, including both the real and imaginary parts, can be obtained by full-wave simulations. This will impose four conditions. We denote the three parameters obtained from the EMT by $\omega_{1,\mathrm{emt}}$, $\omega_{2,\mathrm{emt}}$, and $\gamma_{2,\mathrm{emt}}$, and choose them as the reference values of ω_1, ω_2, and γ_2 of the non-interacting GR and FP modes by allowing a small variation, i.e., $\omega_1 = \omega_{1,\mathrm{emt}} + \Delta\omega_1$, $\omega_2 = \omega_{2,\mathrm{emt}} + \Delta\omega_2$, and $\gamma_2 = \gamma_{2,\mathrm{emt}} + \Delta\gamma_2$. The four aforementioned conditions can be used to fix these parameters since the EMT is a good starting point for the effective Hamiltonian. If the periodic modulation is small ($\varepsilon_2/\varepsilon_1 \approx 1$), the fitting procedure can be further simplified. In this case, the three parameters $\omega_{1,\mathrm{emt}}$, $\omega_{2,\mathrm{emt}}$, and $\gamma_{2,\mathrm{emt}}$ can be directly used without correction, and only two of the four conditions are required to solve the other two parameters γ_1 and κ. Our fitting approach based on the EMT confirms that the condition Eq. (7) holds exactly at the BICs (see Supplement 1, Section 3, for the details of the procedure and examples). This verifies our conclusion that this type of BIC is a form of Friedrich–Wintgen BIC.

At the left side of Fig. 1(b), we schematically show the energy level diagrams and the corresponding reflection spectra of the GR mode (black) and FP mode (red) that give rise to this type of BIC. It is noted that the FP mode corresponds to the peak of the transmission spectra, i.e., the dip of the reflection spectra. A Fano resonance occurs when the GR mode and FP mode are coupled to each other. If the condition Eq. (7) of BIC is satisfied, the linewidth of the Fano resonance vanishes.

From the perspective of Friedrich–Wintgen origin of BIC, the symmetry-protected BIC at the Γ point can also be considered as a result of the coupling of degenerate GR modes [38]. In the effective medium slab, the folded bands of $GM_n^{(-1)}$ and $GM_n^{(+1)}$ at the Γ point give rise to a pair of degenerate states. They have the same frequency ω and decay rate γ, and therefore automatically satisfy the BIC condition in Eq. (2). When this pair of degenerate states are coupled to each other, one of them has a doubled radiation loss while the other becomes the so-called symmetry-protected BIC (see Supplement 1, Section 4, for details). In the middle of the left side of Fig. 1(b) are the energy levels and the corresponding reflection spectra of a pair of degenerate GR modes that result in the symmetry-protected BIC.

Besides the above two types of Friedrich–Wintgen BIC, there exists another type of Friedrich–Wintgen BIC in the PhC slab. It stems from the coupling of two GR modes having the same σ_z symmetry but belonging to different orders, such as $GR_0^{(+1)}$ and $GR_2^{(-1)}$ modes. This type of Friedrich–Wintgen BIC has been discussed in previous studies [23,25]. Normally, because the decay rates of two GR modes are quite close, i.e., $\gamma_1 \sim \gamma_2$, their coupling is likely to lead to an anticrossing effect. Using Eq. (7), it is inferred that $|\Delta\omega_{1,2}| \ll |\kappa|$ and the consequent BIC is located in the vicinity of the anticrossing point, in sharp contrast to the case of accidental BICs at which $|\Delta\omega_{1,2}| \gg |\kappa|$. Therefore, the accidental BICs can deviate from the avoided crossing point considerably and their Friedrich–Wintgen origin is less obvious, so that they are treated as single-resonance modes previously [1,12–14]. The energy levels and the corresponding reflection spectra of the two different GR modes for the conventional Friedrich–Wintgen BICs are shown in the uppermost inset of Fig. 1(b). Thus, the three types of BICs in PhC slabs can all be viewed as the Friedrich–Wintgen-type BIC and can be classified by their origins from the coupling of different modes: (1) GR+FP modes, (2) a pair of degenerate GR modes, and (3) two different GR modes. For any particular band in the PhC slab, with system parameters specified, we can determine the number (n_1, n_2, n_3) of Friedrich–Wintgen BICs of these three types on the band. In fact, this proposed model based on the Friedrich–Wintgen Hamiltonian is general and can also be applied to two-dimensional PhC slabs (see Supplement 1, Section 5, for examples).

B. Global Phase Diagram

In the region with only one radiation channel, as parameters change, BICs move continuously in momentum space. In such cases, the BICs associated with integer topological charges exist robustly, we can use (n_1, n_2, n_3) as indices to define the phase of BIC on the energy band and draw the global phase diagram in the parameter space. When BICs move out of the region with one radiation channel, their numbers (n_1, n_2, n_3) change and a phase transition takes place. It is worth pointing out that when BICs merge or annihilate, the indices (n_1, n_2, n_3) also change

accordingly so that different BIC phases arise. Take the TE mode ($\boldsymbol{E} = E_y \hat{y}$, $\boldsymbol{H} = H_x \hat{x} + H_z \hat{z}$) as an example. The phase diagram for the lowest band–$GR_0^{(-1)}$ is shown in Fig. 1(c). Due to the inversion symmetry, the indices (n_1, n_2, n_3) only cover the BICs on the positive k_x axis of the first Brillouin zone. In the discussion below, we fix the system parameters as $\varepsilon_1 = 1$ and $d = 0.5a$ and vary ε_2 and h, and the presented results for GR and FP modes are from the full-wave simulations unless otherwise specified. In this parameter space, the symmetry-protected BIC due to the coupling of $GR_0^{(-1)}$ and $GR_0^{(+1)}$ modes at Γ point always appears on the lower band. This means that the second index is kept at $n_2 = 1$ and there is no band inversion at the Γ point. In the first Brillouin zone, the $GR_0^{(-1)}$ band is the lowest frequency band and will not intersect with any other GR bands. Therefore, the type of BIC caused by two different GR modes will not appear on the $GR_0^{(-1)}$ band, namely the third index $n_3 = 0$. Furthermore, when the thickness of the PhC slab is very small, the frequency of the FP_2 mode, which has the same σ_z symmetry as the $GR_0^{(-1)}$ mode, is quite high, so that this FP mode will not be coupled with the $GR_0^{(-1)}$ mode to form a BIC. The corresponding band diagram is illustrated in the lowest inset. In this situation, the $GR_0^{(-1)}$ band is kept in $(0, 1, 0)$ phase (the lowest gray area). When slab thickness increases to a critical value (the lowest black solid line), the BIC resulting from the coupling of $GR_0^{(-1)}$ and FP_2 modes appears at the Γ point, and the $GR_0^{(-1)}$ band transfers from $(0, 1, 0)$ phase to $(1, 1, 0)$ phase (the lowest blue area). The band diagram for $(1, 1, 0)$ phase is displayed in the middle inset.

When the slab thickness further increases, high-order FP modes also have redshift, interact with the $GR_0^{(-1)}$ band, and form more BICs. The critical values of slab thicknesses are shown by the other black solid lines. Meanwhile, accidental BICs resulting from the coupling of the GR and FP modes also move toward lower frequency, and eventually fall below the light line and disappear, forming another type of critical line of slab thickness indicated by black dashed lines in Fig. 1(c). We note that as the slab thickness increases, the smaller ε_2 is, the slower the redshift of the FP mode is, so that the BIC resulting from the coupling of the GR mode and lower-order FP mode may coexist with the BIC resulting from the coupling of the GR mode and higher-order FP mode. For example, two accidental BICs caused by FP_{2n} and FP_{2n+2} modes coexist on the $GR_0^{(-1)}$ band and form $(2, 1, 0)$ phase (orange area). Such a case is shown in the uppermost inset of Fig. 1(c). When three and four FP bands interact with the $GR_0^{(-1)}$ band, $(3, 1, 0)$ and $(4, 1, 0)$ phases appear as indicated, respectively, by green and black regions in Fig. 1(c). It is notable that normally there is no merging between the accidental BICs caused by FP modes of different orders on the same GR band. However, on the phase boundaries marked by the black solid lines, the accidental BICs and symmetry-protected BICs merge at the Γ point, which will be described later in detail. It is noted that such phase boundaries are almost flat along the permittivity axis, which reveals a generic property of the at-Γ merging BIC for different optical parameters.

As is mentioned above, the type of BIC resulting from the coupling of two different GR modes does not exist on the $GR_0^{(-1)}$ band, so this part is missing in the phase diagram of Fig. 1(c), while this type of BIC can appear on a higher frequency band, for instance, the $GR_0^{(+1)}$ band. The phase diagram of BICs on this band is shown in Fig. 1(d). The symmetry-protected BIC does not

exist at the Γ point on this band, so there is a region without any BIC, i.e., $(0, 0, 0)$ phase (white area). As slab thickness increases towards the critical line (black dashed), the BIC resulting from the GR and FP modes emerges from the folded light line. As slab thickness further increases to another critical line (black solid), this BIC moves to the Γ point, merges with its symmetrical counterpart on the negative k_x axis, and then deflects onto the k_y axis, which will also be discussed in detail later. When the slab thickness is between the two critical lines, the $GR_0^{(+1)}$ band is in $(1, 0, 0)$ phase (blue area), one example of which is shown in the lowest inset. If the $GR_{2n}^{(-1)}$ ($n \geq 1$) band intersects with and is coupled to the $GR_0^{(+1)}$ band, normally an anticrossing effect occurs, and in the vicinity of the anticrossing point appears the BIC resulting from the coupling of these two GR modes. This type of BIC emerges from the folded light line when the slab thickness is on the critical line (red dashed). As slab thickness increases towards another critical line (red solid), it moves to the Γ point. During this process, the $GR_0^{(+1)}$ band is in a new phase, i.e., $(0, 0, 1)$ phase (green area), one example of which is shown in the middle inset of Fig. 1(d). Since the redshift of the FP mode is larger than that of GR mode when the slab thickness increases, the range of thickness for the existence of BICs resulting from the coupling of two different GR modes is far wider than that for the existence of accidental BICs. When the above two ranges overlap, a new BIC phase arises, $(1, 0, 1)$ phase (purple area). In this type of phase, as shown in the uppermost inset, two different types of Friedrich–Wintgen BICs (BICs resulting from the coupling of two different GR modes and accidental BICs) coexist and may exhibit more interesting phenomena of BICs, such as merging BIC at the off$-\Gamma$ point [23].

C. Charge Dynamics of BICs

The global phase diagrams of BICs give us a clear picture of the charge dynamics of BICs. Here, the dynamics refers to the movement of BICs in the parameter space instead of the time axis. When a phase transition takes place, BICs can merge, emerge, or disappear in momentum space. Figure 2(a) shows the evolution of BICs in the $k_x - h$ space on the $GR_0^{(-1)}$ band when $\varepsilon_2 = 2.1$. As the slab thickness gradually increases, the BIC (red circle) resulting from the coupling of the $GR_0^{(-1)}$ and FP_2 modes moves in the direction of increasing k_x and finally extends to the zone boundary $k_x = \pm\pi/a$. When h increases to a certain critical value, the BIC (green circle) resulting from the coupling of the $GR_0^{(-1)}$ and FP_4 modes appears at the Γ point and then exhibits a similar evolution behavior. These BICs lie close to the trajectory of the intersection point of folded GM_0 and FP_2 (FP_4) bands in the effective medium slab as shown by the red (green) dashed lines. This again manifests the fact that the accidental BICs originate from the coupling of GR and FP modes. The deviation comes from the fact that the intersection points can be treated as nearly the avoided crossing points, which are determined by the non-interacting Hamiltonian. If the Hamiltonian is corrected by considering their coupling, we find that the result (solid lines) coincides with the BICs that obtained from full-wave simulations (circles) in Fig. 2(a).

However, there are two differences between TE polarization and TM polarization. First, compared to TE polarization, BICs resulting from the coupling of the GR and FP modes can exist in a very thin PhC slab ($h/a \sim 0.2$) for TM polarization. Second, there exist at-Γ BICs on the TE band, which are symmetry-protected (black circles). So when evolution trajectories of BICs
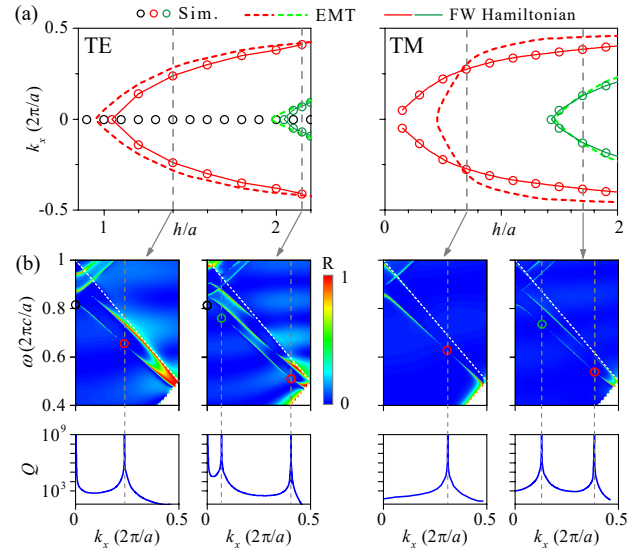

Fig. 2. Evolution of BICs in the $k_x - h$ space. (a) The trajectories (dashed lines) of the intersection point of folded GM_0 and FP bands in the effective medium slab are close to the trajectories (circles) of BICs obtained through full-wave simulation. Red and green color represent the involvement of the FP_2 and FP_4 bands, respectively. The trajectories (solid lines) of BICs obtained through a fitting using Friedrich–Wintgen Hamiltonian coincide with the simulated results. (b) For TE (TM) polarization, the simulated reflection spectra of the PhC slab at $h/a = 1.4$ and 2.15 (0.9 and 1.7) are shown to exhibit different BIC phases. White dashed lines denote the folded light lines. The vanishing points of Fano peaks shown by circles in the spectra represent BICs on the $GR_0^{(-1)}$ band, the color of which is the same as that in (a). The corresponding Q factors of the $GR_0^{(-1)}$ band are shown in the lower panels to verify the existence of BICs. Here, the other system parameters are the same as those in Fig. 1, and $\varepsilon_2 = 2.1$.

intersect with the axis $k_x = 0$, on the TE band, BICs of different types merge at $h/a = 1.044$ and 2.045, while on the TM band, BICs of the same type merge at $h/a = 1.447$. These two types of merging correspond to different BIC phase transitions. For demonstration, we show reflection spectra and Q factors of the $GR_0^{(-1)}$ band in two different BIC phases in Fig. 2(b). As the slab thickness decreases, the TE band changes from $(2, 1, 0)$ phase into $(1, 1, 0)$ phase and the TM band from $(2, 0, 0)$ into $(1, 0, 0)$.

To further study charge dynamics in the vicinity of the Γ point, we show the band structures and far-field polarization maps of the $GR_0^{(-1)}$ band in Fig. 3, where there are three different types of evolutions of BICs. The Q factors of $GR_0^{(-1)}$ modes are shown as background. Note that the topological charge is defined by $v = (1/2\pi) \oint_L d\mathbf{k}_\parallel \cdot \nabla_{\mathbf{k}_\parallel} \psi(\mathbf{k}_\parallel)$.

Here, L is a closed loop in momentum space surrounding the singular point in the counterclockwise direction, and $\psi(\mathbf{k}_\parallel) = 1/2 \arg[S_1(\mathbf{k}_\parallel) + i S_2(\mathbf{k}_\parallel)]$ is the orientation angle of the polarization state, where S_i is the Stokes parameter of the far-field polarization vector. For the TE mode, the $GR_0^{(-1)}$ and FP_2 modes are coupled to each other to produce an off$-\Gamma$ BIC with $v = -1$ on the positive k_x axis, as shown in Fig. 3(a). Due to the inversion symmetry of the system, there is an identical off$-\Gamma$ BIC with $v = -1$ on the negative k_x axis. As the slab thickness decreases, a blue shift occurs on the FP_2 band, and this causes the off$-\Gamma$ BICs to gradually move towards the Γ point. When $h = 1.0424a$, they merge with the symmetry-protected BIC with
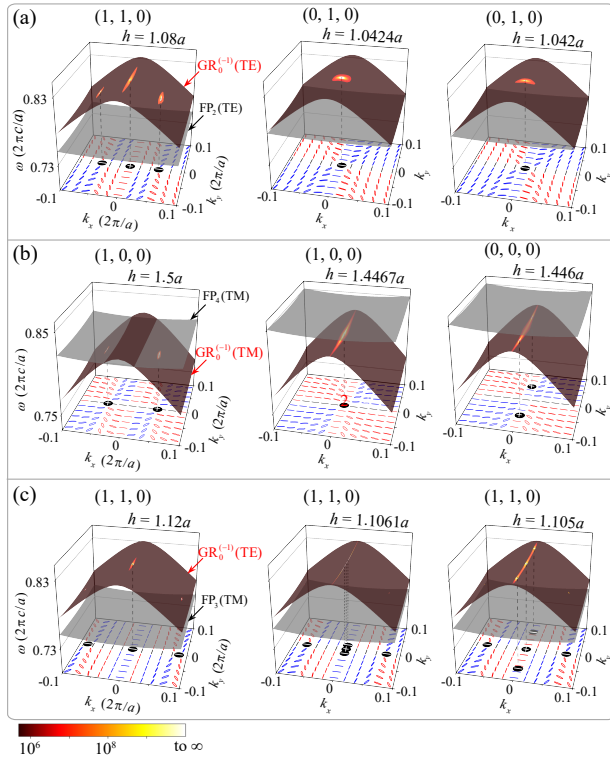
Fig. 3. Examples of charge dynamics of BICs in the vicinity of the Γ point. (a) Evolution of the BIC resulting from the coupling of the TE-polarized $GR_0^{(-1)}$ and FP_2 modes as slab thickness changes. The simulated band structures of $GR_0^{(-1)}$ and FP modes are both plotted. The Q factors of $GR_0^{(-1)}$ modes are shown on the band structure in color scale. A pair of off $-\Gamma$ BICs with $v = -1$ and a symmetry-protected BIC with $v = +1$ merge at the Γ point. The numbers (n_1, n_2, n_3) at the top of each figure represent BIC phases of the $GR_0^{(-1)}$ band on the positive k_x axis. (b) Evolution of the BIC resulting from the coupling of the TM-polarized $GR_0^{(-1)}$ and FP_4 modes as the slab thickness changes. A pair of off $-\Gamma$ BICs with $v = +1$ merge at the Γ point to form a BIC with $v = +2$, which then splits into a pair of BICs with $v = +1$ moving along the k_y axis. (c) Coupling of the TE-polarized $GR_0^{(-1)}$ mode and TM-polarized FP_3 mode with slab thickness changing. When $h \leq 1.1061a$, the two modes are coupled to each other and produce a pair of BICs with $v = -1$ on the k_y axis. The off $-\Gamma$ BICs with $v = -1$ on the k_x axis are not involved in this charge splitting process. Here, the other system parameters are the same as those in Fig. 2.

$v = +1$ to form a BIC with $v = -1$ at the Γ point. As the slab thickness further decreases, off $-\Gamma$ BICs will not deflect onto the k_y axis. This is because for TE-like modes on the k_y axis, far-field radiation of the $GR_0^{(-1)}$ mode is x-polarized and far-field radiation of the FP_2 mode is y-polarized, so they cannot destructively interfere with each other to produce BICs (see Fig. S10 in Supplement 1 for details). In this evolution, the $GR_0^{(-1)}$ band changes from $(1, 1, 0)$ to $(0, 1, 0)$ phase.

Similarly, in the case of the TM mode, we still take the $GR_0^{(-1)}$ mode for example. This mode couples to the FP_4 mode to produce an off $-\Gamma$ BIC with $v = +1$ on the positive k_x axis, as shown in Fig. 3(b). As the slab thickness decreases to $h = 1.4467a$, this off $-\Gamma$ BIC merges with its counterpart on the negative k_x axis to form a BIC with $v = +2$ at the Γ point. This topological charge $v = +2$ is allowed by the symmetry of the system [7]. However, unlike the situation in the TE case, the far-field radiations of

TM-like $GR_0^{(-1)}$ mode and FP_4 mode on the k_y axis are both x-polarized, and they can destructively interfere with each other to produce a BIC. This means the resultant at-Γ BIC with $v = +2$ is not stable. As the slab thickness continues to decrease, it splits into a pair of BICs with $v = +1$ that move along the k_y axis. During this evolution, the BIC phase of the $GR_0^{(-1)}$ band changes from $(1, 0, 0)$ to $(0, 0, 0)$ since the indices of phase here are defined on the positive k_x axis. It is obvious that our classification of BIC phases is also applicable to the k_y axis and even the whole momentum space. For instance, if the first quadrant of momentum space is considered, the BIC phase remains unchanged, i.e., $(1, 0, 0)$ phase. We choose the positive k_x axis in this study only because most previous studies focus on this axis [6,7,9,21,25,30].

The above two types of BIC evolution stem from the interaction between the GR mode and the FP mode, which have the same polarization. In fact, the GR mode and the FP mode, which are differently polarized, can also interact and cause BICs to evolve. In Fig. 3(c), we take TE-polarized $GR_0^{(-1)}$ and TM-polarized FP_3 modes as an example. On the k_x axis, they are completely orthogonal in polarization and hence are not coupled to each other. However, on the k_y axis, they have the same σ_z symmetry and their far-field radiations are both x-polarized, so they may destructively interfere with each other to produce a BIC. Here, when $h \leq 1.1061a$, a pair of BICs with $v = -1$ appears on the k_y axis while the topological charge carried by the symmetry-protected BIC changes from -1 to $+1$. In this evolution, the phase of the $GR_0^{(-1)}$ band remains unchanged, i.e., $(1, 1, 0)$ since we only consider the positive k_x axis. If the first quadrant of momentum space is considered, the BIC phase changes from $(1, 1, 0)$ to $(2, 1, 0)$.

The phenomenon of charge splitting shown in Fig. 3(c) has not been reported previously. Such kind of charge dynamics is a natural result from the viewpoint of the interaction between GR and FP modes. Whether BICs exist or not can be estimated through the polarization analysis of their far-field radiations. It is also worth noting that in the charge dynamics considered above, the FP mode plays a critical role. We can use EMT to estimate the change of the FP mode when the system parameters change, allowing us to trace accidental BICs along the intersection points as indicated in Fig. 2, which can provide guidance for experimental designs.

3. EXPERIMENTAL OBSERVATION

To verify the phase diagram of BICs above, we experimentally observed the phase and phase transitions of BICs. As the aspect ratio (h/a) is high, experimental samples are difficult to fabricate and may exhibit a tapering shape. In order to make the sample fabrication easier, we adopt a structure similar to PhC slab in the experiment, i.e., the combination of a grating with small thickness and a high-index uniform slab. As shown in Fig. 4(a), the high-index slab is made of SiO_2 with a thickness h, and the grating consists of an array of polymethyl methacrylate (PMMA) with a refractive index of 1.5, a thickness of $h_g = 100$ nm, a periodicity of $a = 400$ nm, and an etching width of $d = 200$ nm. Using metal substrate (a 240-nm-thick silver film evaporated on a glass substrate) as a reflecting mirror, we can further reduce the thickness of the whole structure. In order to prevent oxidation of the silver film, a layer of 25 nm Al_2O_3 is introduced between the silver film and SiO_2 slab (see Supplement 1, Section 9, for the details of sample fabrication). Due to the periodicity of the PMMA array, the bands of waveguide modes in the SiO_2 slab are folded into the
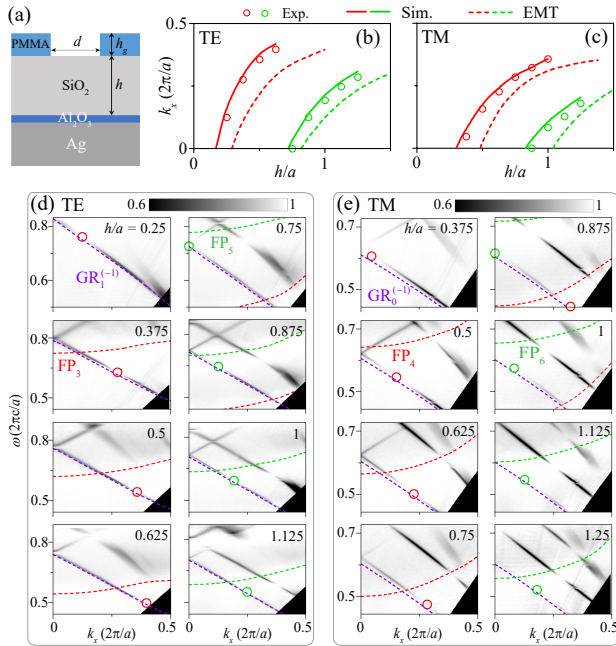
Fig. 4. Experimental observation of charge dynamics of BICs in the $k_x - h$ space. (a) Sketch of the experimental structure, where period $a = 400$ nm, $d = 200$ nm, and $h_g = 100$ nm. (b),(c) Experimentally observed (circles) and simulated trajectories (solid lines) of the BICs caused by FP modes of different orders on the TE-polarized $GR_1^{(-1)}$ and TM-polarized $GR_0^{(-1)}$ bands. The trajectories of the intersection points of the corresponding folded GM and FP bands in the effective medium slab are also marked by the red and green dashed lines, respectively. (d),(e) Experimentally observed reflection spectra of the structure with different h for TE and TM polarization. The points in circles represent accidental BICs on the TE-polarized $GR_1^{(-1)}$ or TM-polarized $GR_0^{(-1)}$ band, the simulated results of which are indicated by the purple dashed lines. The simulated FP bands are marked by the red and green dashed lines, the colors of which correspond to the resultant BICs. The black areas at the lower right corner are those which cannot be measured due to limitations of the numerical apertures of the objective lens.

continuum and hence radiate into free space, making it possible for us to observe $GR_n^{(m)}$ bands. Owing to the introduction of the metal mirror, the effective slab thickness is doubled. However, only the modes that have zero transverse component of the electric field at the mirror surface survive, that is, the TE-polarized $GR_{2n+1}^{(m)}$ mode or the TM-polarized $GR_{2n}^{(m)}$ mode.

As discussed above, these GR modes can couple to the FP modes with the same symmetry and, as a result, produce BICs under specific parameters. To observe the evolution trajectories of BICs in this type of structure, we employ momentum-space imaging spectroscopy [8] to obtain polarization-dependent angle-resolved reflectance spectra, TE and TM polarizations of which are shown in Fig. 4(d) and 4(e), respectively. Here, we focus on the BICs on TE-polarized $GR_1^{(-1)}$ and TM-polarized $GR_0^{(-1)}$ bands, as indicated by the red and green dots. The corresponding simulated dispersion curves (purple dashed lines) are shown in Figs. 4(d) and 4(e), agreeing well with the measured spectra. It is noted that the other vanishing points of reflection dip in the measured spectra correspond to the BICs on the higher-frequency bands. As the thickness h of the SiO_2 slab gradually increases, a redshift of frequency of the FP bands (red and green dashed lines) occurs, which causes BICs to move in the direction of increasing k_x. The observed
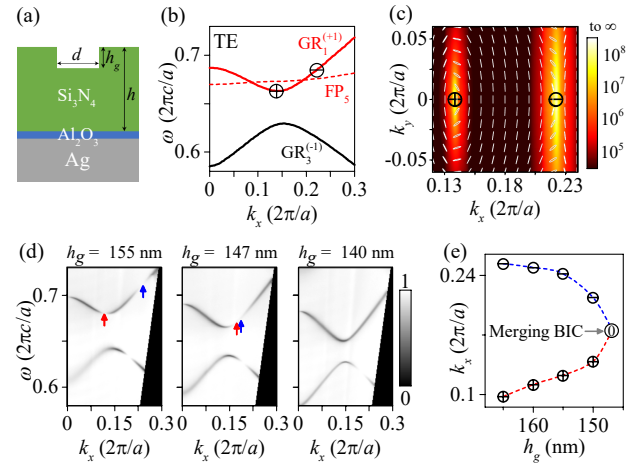
trajectories of BICs in the $k_x - h$ space exactly fit the simulated ones, as shown in Figs. 4(b) and 4(c). Moreover, these BICs lie close to the trajectory of the intersection points of the corresponding folded GM and FP bands obtained by the EMT as shown by the red and green dashed lines. This verifies the Friedrich–Wintgen origin as well as the charge dynamics of accidental BICs we depict in Fig. 2.

We further construct a more interesting merging BIC at the off−Γ point based on the phase diagrams in Fig. 1(d). In experiments, we still use the structure shown in Fig. 4 but replace the layers of SiO_2 and PMMA with Si_3N_4 layers, as shown in Fig. 5(a). In Fig. 5(b), there exists a BIC with $v = +1$ and a BIC with $v = -1$ on the TE-polarized $GR_1^{(+1)}$ band, and their topological charges are shown in the far-field polarization map in Fig. 5(c). The BIC with $v = +1$ results from the coupling of the $GR_1^{(+1)}$ and $GR_3^{(-1)}$ modes and is located in the vicinity of the anticrossing point of these two bands. Yet the BIC with $v = -1$ results from the coupling of the $GR_1^{(+1)}$ and FP_5 modes, and as structural parameters change, it moves in tandem with the movement of the FP_5 band. In this experiment, we keep the thicknesses of the whole Si_3N_4 layer the same, and adjust the effective relative permittivity ε_{eff} by changing etching depth h_g in the Si_3N_4 layer. As h_g decreases, ε_{eff} increases gradually and a redshift occurs in the FP_5 band. This causes the BIC with $v = -1$ to move toward the BIC with $v = 1$ to form a merging BIC, which is finally annihilated. The experimentally obtained reflection spectra of the structure with different h_g in Fig. 5(d) clearly show the merging process of the two BICs with opposite topological charges. More measured reflection spectra are also given in Fig. S12. The evolution trajectories of the two BICs in the $k_x - h$ space are shown in Fig. 5(e), which terminate at their intersection point and form a merging BIC.

Fig. 5. Experimental observation of BICs merging at off−Γ point. (a) Sketch of the structure. (b) Simulated band structure. On the TE-polarized $GR_1^{(+1)}$ band, there exist two BICs with opposite topological charges, which result from the coupling of the $GR_1^{(+1)}$ and $GR_3^{(-1)}$ (or FP_5) modes. (c) Far-field polarization map of $GR_1^{(+1)}$ band with the radiation Q factor as the background. (d) Experimentally observed reflection spectra with different h_g. The two BICs with opposite charges are marked by the red and blue arrows. As h_g decreases, the two BICs gradually move close to and merge with each other, and then are annihilated. (e) Evolution trajectories of the two BICs. Here, the structural parameters are chosen as $h = 350$ nm, $d = 130$ nm and the other parameters are the same as those in Fig. 4.

4. CONCLUSION

It is demonstrated that all the three types of BICs in the PhC slab are Friedrich–Wintgen-type BICs, in the sense that the far-field radiation is suppressed by the interference of two degrees of freedom. Each category of BIC has its own Friedrich–Wintgen origin: the accidental BIC stems from the coupling of the GR and FP modes; the symmetry-protected BIC the coupling of a pair of degenerate GR modes at the Γ point; and the conventional Friedrich–Wintgen BIC the coupling of two different GR modes. Based on the three Friedrich–Wintgen origins of BICs, the global phase diagram of BICs can be obtained for each band in the parameter space, and their evolution in momentum space can be revealed using the phase diagram. As system parameters change, BICs resulting from the coupling of the GR and FP modes move alongside the movement of the FP mode. A new phase will appear when they merge with different types of BICs, including BICs of the same type (their symmetrical counterparts in momentum space) or the symmetry-protected BIC at the Γ point, or the BICs resulting from the coupling of two different GR modes at the off $-\Gamma$ point. We further experimentally observe the phase transitions and critical points of BICs, including their merging process at the off $-\Gamma$ point. The finding that the BICs originate from different manifestations of the Friedrich–Wintgen mechanism and their corresponding phase diagrams can deepen our understanding of BICs and provide guidance for experimental designs and practical applications.

Disclosures. The authors declare no conflicts of interest.

Data availability. Data underlying the results presented in this paper are not publicly available at this time but may be obtained from the authors upon reasonable request.

Supplemental document. See Supplement 1 for supporting content.

†These authors contributed equally to this paper.

REFERENCES

1. C. W. Hsu, B. Zhen, A. D. Stone, J. D. Joannopoulos, and M. Soljačić, "Bound states in the continuum," Nat. Rev. Mater. **1**, 1–13 (2016).
2. K. Koshelev, A. Bogdanov, and Y. Kivshar, "Meta-optics and bound states in the continuum," Sci. Bull. **64**(12), 836–842 (2019).
3. A. F. Sadreev, "Interference traps waves in an open system: bound states in the continuum," Rep. Prog. Phys. **84**, 055901 (2021).
4. J. von Neuman and E. Wigner, "Über merkwürdige diskrete Eigenwerte," Phys. Z. **30**, 465–467 (1929).
5. H. Friedrich and D. Wintgen, "Interfering resonances and bound states in the continuum," Phys. Rev. A **32**, 3231–3242 (1985).
6. C. W. Hsu, B. Zhen, J. Lee, S. L. Chua, S. G. Johnson, J. D. Joannopoulos, and M. Soljacic, "Observation of trapped light within the radiation continuum," Nature **499**, 188–191 (2013).
7. B. Zhen, C. W. Hsu, L. Lu, A. D. Stone, and M. Soljacic, "Topological nature of optical bound states in the continuum," Phys. Rev. Lett. **113**, 257401 (2014).
8. Y. Zhang, A. Chen, W. Liu, C. W. Hsu, B. Wang, F. Guan, X. Liu, L. Shi, L. Lu, and J. Zi, "Observation of polarization vortices in momentum space," Phys. Rev. Lett. **120**, 186103 (2018).
9. H. M. Doeleman, F. Monticone, W. den Hollander, A. Alù, and A. F. Koenderink, "Experimental observation of a polarization vortex at an optical bound state in the continuum," Nat. Photonics **12**, 397–401 (2018).
10. E. N. Bulgakov and A. F. Sadreev, "Bloch bound states in the radiation continuum in a periodic array of dielectric rods," Phys. Rev. A **90**, 053801 (2014).
11. L. Yuan and Y. Y. Lu, "Bound states in the continuum on periodic structures surrounded by strong resonances," Phys. Rev. A **97**, 043828 (2018).
12. Y. Yang, C. Peng, Y. Liang, Z. Li, and S. Noda, "Analytical perspective for bound states in the continuum in photonic crystal slabs," Phys. Rev. Lett. **113**, 037401 (2014).
13. X. Gao, C. W. Hsu, B. Zhen, X. Lin, J. D. Joannopoulos, M. Soljacic, and H. Chen, "Formation mechanism of guided resonances and bound states in the continuum in photonic crystal slabs," Sci. Rep. **6**, 31908 (2016).
14. S. Dai, L. Liu, D. Han, and J. Zi, "From topologically protected coherent perfect reflection to bound states in the continuum," Phys. Rev. B **98**, 081405 (2018).
15. A. Cerjan, C. W. Hsu, and M. C. Rechtsman, "Bound states in the continuum through environmental design," Phys. Rev. Lett. **123**, 023902 (2019).
16. W. Chen, Y. Chen, and W. Liu, "Singularities and poincare indices of electromagnetic multipoles," Phys. Rev. Lett. **122**, 153907 (2019).
17. X. Gao, B. Zhen, M. Soljačić, H. Chen, and C. W. Hsu, "Bound states in the continuum in fiber bragg gratings," ACS Photon. **6**, 2996–3002 (2019).
18. Q. Song, J. Hu, S. Dai, C. Zheng, D. Han, J. Zi, Z. Q. Zhang, and C. T. Chan, "Coexistence of a new type of bound state in the continuum and a lasing threshold mode induced by PT symmetry," Sci. Adv. **6**, eabc1160 (2020).
19. Y. Plotnik, O. Peleg, F. Dreisow, M. Heinrich, S. Nolte, A. Szameit, and M. Segev, "Experimental observation of optical bound states in the continuum," Phys. Rev. Lett. **107**, 183901 (2011).
20. J. Lee, B. Zhen, S. L. Chua, W. Qiu, J. D. Joannopoulos, M. Soljacic, and O. Shapira, "Observation and differentiation of unique high-Q optical resonances near zero wave vector in macroscopic photonic crystal slabs," Phys. Rev. Lett. **109**, 067401 (2012).
21. J. Jin, X. Yin, L. Ni, M. Soljacic, B. Zhen, and C. Peng, "Topologically enabled ultrahigh-Q guided resonances robust to out-of-plane scattering," Nature **574**, 501–504 (2019).
22. T. Yoda and M. Notomi, "Generation and annihilation of topologically protected bound states in the continuum and circularly polarized states by symmetry breaking," Phys. Rev. Lett. **125**, 053902 (2020).
23. M. Kang, S. Zhang, M. Xiao, and H. Xu, "Merging bound states in the continuum at off-high symmetry points," Phys. Rev. Lett. **126**, 117402 (2021).
24. M. V. Rybin, K. L. Koshelev, Z. F. Sadrieva, K. B. Samusev, A. A. Bogdanov, M. F. Limonov, and Y. S. Kivshar, "High-Q supercavity modes in subwavelength dielectric resonators," Phys. Rev. Lett. **119**, 243901 (2017).
25. E. N. Bulgakov and D. N. Maksimov, "Avoided crossings and bound states in the continuum in low-contrast dielectric gratings," Phys. Rev. A **98**, 053840 (2018).
26. E. N. Bulgakov and A. F. Sadreev, "Bound states in the continuum in photonic waveguides inspired by defects," Phys. Rev. B **78**, 075105 (2008).
27. D. C. Marinica, A. G. Borisov, and S. V. Shabanov, "Bound states in the continuum in photonics," Phys. Rev. Lett. **100**, 183902 (2008).
28. S. Weimann, Y. Xu, R. Keil, A. E. Miroshnichenko, A. Tunnermann, S. Nolte, A. A. Sukhorukov, A. Szameit, and Y. S. Kivshar, "Compact surface Fano states embedded in the continuum of waveguide arrays," Phys. Rev. Lett. **111**, 240403 (2013).
29. A. A. Lyapina, D. N. Maksimov, A. S. Pilipchuk, and A. F. Sadreev, "Bound states in the continuum in open acoustic resonators," J. Fluid Mech. **780**, 370–387 (2015).
30. S. I. Azzam, V. M. Shalaev, A. Boltasseva, and A. V. Kildishev, "Formation of bound states in the continuum in hybrid plasmonic-photonic systems," Phys. Rev. Lett. **121**, 253901 (2018).
31. B. E. A. Saleh and M. C. Teich, *Fundamentals of Photonics*, 3rd ed. (Wiley, 2019).
32. S. Fan and J. D. Joannopoulos, "Analysis of guided resonances in photonic crystal slabs," Phys. Rev. B **65**, 235112 (2002).

33. W. Suh, Z. Wang, and S. H. Fan, "Temporal coupled-mode theory and the presence of non-orthogonal modes in lossless multimode cavities," IEEE J. Quantum Electron. **40**, 1511–1518 (2004).

34. I. Rotter, "A continuum shell model for the open quantum mechanical nuclear system," Rep. Prog. Phys. **54**, 635–682 (1991).

35. C. W. Hsu, B. Zhen, M. Soljačić, and A. D. Stone, "Polarization state of radiation from a photonic crystal slab," arXiv, arXiv:1708.02197 (2017).

36. P. Sheng, *Introduction to Wave Scattering, Localization and Mesoscopic Phenomena*, 2nd ed. (Springer, 2006).

37. A. Abdrabou and Y. Y. Lu, "Indirect link between resonant and guided modes on uniform and periodic slabs," Phys. Rev. A **99**, 063818 (2019).

38. K. Koshelev, A. Bogdanov, and Y. Kivshar, "Engineering with bound states in the continuum," Opt. Photon. News **31**(1), 38–45 (2020).